

Two- and three-point functions at criticality: Monte Carlo simulations of the improved three-dimensional Blume-Capel model

Martin Hasenbusch*

*Institut für Physik, Humboldt-Universität zu Berlin,
Newtonstr. 15, 12489 Berlin, Germany*

(Dated: September 27, 2018)

Abstract

We compute two- and three-point functions at criticality for the three-dimensional Ising universality class. To this end we simulate the improved Blume-Capel model at the critical temperature on lattices of a linear size up to $L = 1600$. As check also simulations of the spin-1/2 Ising model are performed. We find $f_{\sigma\sigma\epsilon} = 1.051(1)$ and $f_{\epsilon\epsilon\epsilon} = 1.533(5)$ for operator product expansion coefficients. These results are consistent with but less precise than those recently obtained by using the bootstrap method. An important ingredient in our simulations is a variance reduced estimator of N -point functions. Finite size corrections vanish with $L^{-\Delta_\epsilon}$, where L is the linear size of the lattice and Δ_ϵ is the scaling dimension of the leading Z_2 -even scalar ϵ .

PACS numbers: 05.50.+q, 05.70.Jk, 05.10.Ln

* Martin.Hasenbusch@physik.hu-berlin.de

I. INTRODUCTION

Recently we have seen enormous progress in the understanding of critical phenomena in three dimensions by using the conformal bootstrap approach [1–4], to give only a few references. For a recent lecture note on the subject see [5]. In particular, precise numbers for scaling dimensions and operator product expansion (OPE) coefficients for the universality class of the three-dimensional Ising model were obtained. For a very detailed account see ref. [4].

The functional form of two-point functions of primary operators is fixed by conformal invariance

$$\langle \mathcal{O}_1(x_1) \mathcal{O}_2(x_2) \rangle = \frac{C_1 \delta_{\Delta_1, \Delta_2}}{|x_1 - x_2|^{2\Delta_1}} \quad , \quad (1)$$

where \mathcal{O}_i is the operator taken at the site x_i and Δ_i is its scaling dimension. The scaling dimensions of the leading Z_2 -odd scalar σ and the leading Z_2 -even scalar ϵ for the three-dimensional Ising universality class are $\Delta_\sigma = 0.5181489(10)$ and $\Delta_\epsilon = 1.412625(10)$, respectively [3, 4]. The critical exponents that are usually discussed in critical phenomena can be deduced from these two scaling dimensions. Let us consider two examples: The exponent $\eta = d + 2 - 2y_h = d + 2 - 2(d - \Delta_\sigma) = 2\Delta_\sigma - d + 2 = 0.0362978(20)$ governs the decay of the spin-spin correlation function at the critical point, where y_h is the RG-exponent related to the external field and d is the dimension of the system. The critical exponent of the correlation length is given by $\nu = 1/y_t = 1/(d - \Delta_\epsilon) = 0.6299709(40)$, where y_t is the RG-exponent related to the temperature. In table 2 of [4] one finds $\omega = \Delta_{\epsilon'} - 3 = 0.82968(23)$ for the exponent of the leading correction. These results are by far more accurate than previous ones obtained by other methods. For example using Monte Carlo simulations of the improved Blume-Capel model $\nu = 0.63002(10)$, $\eta = 0.03627(10)$, and $\omega = 0.832(6)$ had been obtained [6]. Results obtained from high-temperature series expansions, see for example refs. [7, 8], are slightly less accurate than those from Monte Carlo simulations. Field theoretic methods, see for example ref. [9], give even less precise estimates. In our numerical study, corrections caused by the breaking of the rotational symmetry are an important issue. These are governed by the correction exponent ω_{NR} . In table I of ref. [7] the authors quote $\omega_{NR} = 2.0208(12)$, which is in reasonable agreement with $\omega_{NR} = 2.022665(28)$ that follows from $\Delta = 5.022665(28)$ for angular momentum $l = 4$ given in table 2 of ref. [4]. There is a very rich literature on critical phenomena, which we can not recapitulate here. We refer the

reader to reviews of the subject [10–13].

Now let us turn to the OPE coefficients. Also the form of three-point functions is fixed by conformal invariance. Normalizing the operators such that $C_i = 1$, eq. (1), one gets [14]

$$\langle \mathcal{O}_1(x_1) \mathcal{O}_2(x_2) \mathcal{O}_3(x_3) \rangle = \frac{f_{123}}{|x_1 - x_2|^{\Delta_1 + \Delta_2 - \Delta_3} |x_2 - x_3|^{\Delta_2 + \Delta_3 - \Delta_1} |x_3 - x_1|^{\Delta_3 + \Delta_1 - \Delta_2}} , \quad (2)$$

where the OPE coefficients f_{123} depend on the universality class. Using the conformal bootstrap method, highly accurate results for OPE coefficients of the Ising universality class in three dimensions were obtained [3, 4]:

$$f_{\sigma\sigma\epsilon} = 1.0518537(41) \quad (3)$$

and

$$f_{\epsilon\epsilon\epsilon} = 1.532435(19) . \quad (4)$$

Until recently, there had been no results obtained by other methods that could be compared with eqs. (3,4). In particular in Monte Carlo simulations of lattice models, it is unclear how an infinite volume at the critical point could be well approximated.

In ref. [15] the requirement of an infinite volume was circumvented by studying two-point correlators at the critical temperature applying a finite external field h . The OPE coefficients are obtained from the h -dependence of the two-point correlators. For details of the method we refer the reader to ref. [15]. Simulating the Ising model on a simple cubic lattice, the authors find

$$f_{\sigma\sigma\epsilon} = 1.07(3) , f_{\epsilon\epsilon\epsilon} = 1.45(30) . \quad (5)$$

These estimates were improved by using a trapping potential in ref. [16]:

$$f_{\sigma\sigma\epsilon} = 1.051(3) , f_{\epsilon\epsilon\epsilon} = 1.32(15) . \quad (6)$$

Very recently, Herdeiro [17] computed two- and three-point functions for the Ising model on the simple cubic lattice at the critical point, using the so called UV-sampler method. The method had been tested at the example of the Ising model on the square lattice [18]. Fitting his data for the three-point function with a one parameter Ansatz, fixing Δ_σ and Δ_ϵ to their bootstrap values, Herdeiro gets

$$f_{\sigma\sigma\epsilon} = 1.05334(203) , f_{\epsilon\epsilon\epsilon} = 1.578(27) . \quad (7)$$

Here we shall follow a different strategy. We simulated the improved Blume-Capel model at the critical point on a simple cubic lattice with periodic boundary conditions. To keep finite size effects small, we simulated lattices of a linear size up to $L = 1600$. Furthermore an extrapolation in the lattice size is performed. It turns out that finite size effects at the critical point are $\propto L^{-\Delta_\epsilon}$ for all quantities that we study here. We employ variance reduction as proposed in refs. [19, 20]. This is in particular helpful in the case of the $\epsilon\epsilon\epsilon$ function.

The outline of the paper is the following: In the next section we recall the definition of the Blume-Capel model and summarize briefly the results of ref. [6]. Then we define the two- and three-point functions that we measure. Then in section IV we discuss the finite size scaling behaviour of the quantities that we study. In sections V we discuss the application of the variance reduction method to our problem. Next we discuss the simulations that we perform. It follows the analysis of the data. Finally we conclude and give an outlook.

II. THE MODEL

As in previous work, we study the Blume-Capel model on the simple cubic lattice. For a vanishing external field, it is defined by the reduced Hamiltonian

$$H = -\beta \sum_{\langle xy \rangle} s_x s_y + D \sum_x s_x^2, \quad (8)$$

where the spin might assume the values $s_x \in \{-1, 0, 1\}$. $x = (x^{(0)}, x^{(1)}, x^{(2)})$ denotes a site on the simple cubic lattice, where $x^{(i)} \in \{0, 1, \dots, L_i - 1\}$ and $\langle xy \rangle$ denotes a pair of nearest neighbours on the lattice. In this study we consider $L_0 = L_1 = L_2 = L$ throughout. The inverse temperature is denoted by $\beta = 1/k_B T$. The partition function is given by $Z = \sum_{\{s\}} \exp(-H)$, where the sum runs over all spin configurations. The parameter D controls the density of vacancies $s_x = 0$. In the limit $D \rightarrow -\infty$ vacancies are completely suppressed and hence the spin-1/2 Ising model is recovered.

In $d \geq 2$ dimensions the model undergoes a continuous phase transition for $-\infty \leq D < D_{tri}$ at a β_c that depends on D , while for $D > D_{tri}$ the model undergoes a first order phase transition, where $D_{tri} = 2.0313(4)$ for $d = 3$, see ref. [21].

Numerically, using Monte Carlo simulations it has been shown that there is a point $(D^*, \beta_c(D^*))$ on the line of second order phase transitions, where the amplitude of leading corrections to scaling vanishes. We refer to the Blume-Capel model at values of D that are

good numerical approximations of D^* as improved Blume-Capel model. For a more general discussion of improved models see for example section 3.5 of [22] or section 2.3.1 of [13]. In [6] we simulated the model at $D = 0.655$ close to β_c on lattices of a linear size up to $L = 360$. We obtained $\beta_c(0.655) = 0.387721735(25)$ and $D^* = 0.656(20)$. The amplitude of leading corrections to scaling at $D = 0.655$ is at least by a factor of 30 smaller than for the spin-1/2 Ising model.

Here we simulate the Blume-Capel model at $D = 0.655$. Most of our simulations are performed at $\beta = 0.387721735$. In order to check the sensitivity of the results on β , we performed in addition a few simulations at $\beta = 0.38772$ and 0.38772347 . In order to check the effect of leading corrections to scaling we also simulated the spin-1/2 Ising model on the simple cubic lattice at $\beta = 0.22165462$. Note that in eq. (A2) of ref. [23] we quote $\beta_c = 0.22165462(2)$.

III. THE OBSERVABLES

On the lattice we identify

$$\epsilon(x) = s_x^2 - \langle s_x^2 \rangle + \dots \quad (9)$$

$$\sigma(x) = s_x + \dots, \quad (10)$$

where in our numerical study $\langle s_x^2 \rangle$ is replaced by its estimate obtained from the given simulation at finite L . Corrections are caused by fields with the same symmetry properties but higher dimensions.

In the case of the Ising model, eq. (9) makes no sense. In the literature $s_x s_y$, where x and y are nearest neighbours, is used instead of s_x^2 . Here, motivated by eq. (33) below, we used S_x^2 , where $S_x = \sum_{y.nn.x} s_y$, where $y.nn.x$ means that y is a nearest neighbour of x .

In order to keep the study tractable, we have to single out a few directions for the displacements between the points. In the case of the two-point functions we consider displacements along the axes

$$x_2 - x_1 = (j, 0, 0) \quad , \quad x_2 - x_1 = (0, j, 0) \quad , \quad x_2 - x_1 = (0, 0, j) \quad , \quad (11)$$

the face diagonals

$$\begin{aligned} x_2 - x_1 &= (j, j, 0) \quad , \quad x_2 - x_1 = (j, 0, j) \quad , \quad x_2 - x_1 = (0, j, j) \quad , \\ x_2 - x_1 &= (j, -j, 0) \quad , \quad x_2 - x_1 = (j, 0, -j) \quad , \quad x_2 - x_1 = (0, j, -j) \quad , \end{aligned} \quad (12)$$

and space diagonals

$$x_2 - x_1 = (j, j, j) \quad , \quad x_2 - x_1 = (j, j, -j) \quad , \quad x_2 - x_1 = (j, -j, j) \quad , \quad x_2 - x_1 = (j, -j, -j) \quad , \quad (13)$$

where j is an integer. In the following we shall indicate these three directions by axis (a), face diagonal (f), and space diagonal (d), respectively. In our simulation program we summed over all choices that are related by symmetry to reduce the statistical error. In particular, we summed over all possible choices of x_1 . In the following we shall denote the two-point function by $g_{r,\mathcal{O}_1,\mathcal{O}_2}(x)$, where $r \in \{a, f, d\}$ gives the direction and $x = |x_1 - x_2|$ is the distance between the two points.

In the discussion of our numerical results we are a bit sloppy with the notation and use g also for the numerical estimates obtained from the simulation. Hence there might be also a dependence on the linear lattice size that is not indicated explicitly.

In the case of the three-point functions

$$G_{r,\mathcal{O}_1,\mathcal{O}_2,\mathcal{O}_3}(x) = \langle \mathcal{O}_1(x_1) \mathcal{O}_2(x_2) \mathcal{O}_3(x_3) \rangle \quad (14)$$

we study the two choices $\mathcal{O}_1 = \mathcal{O}_2 = \sigma$ and $\mathcal{O}_3 = \epsilon$ and $\mathcal{O}_1 = \mathcal{O}_2 = \mathcal{O}_3 = \epsilon$. Furthermore, we consider two different geometries that are indicated by r . For $r = f$ the largest displacement is along a face diagonal. For example

$$x_3 - x_1 = (j, 0, 0) \quad , \quad x_3 - x_2 = (0, j, 0) \quad . \quad (15)$$

Our second choice is indicated by $r = d$ and the largest displacement is along a space diagonal. For example

$$x_3 - x_1 = (j, 0, 0) \quad , \quad x_3 - x_2 = (0, j, j) \quad , \quad (16)$$

where j is integer and also here we sum in our simulation over all choices that are related by symmetry to reduce the statistical error. The argument x of G gives the largest distance between two points $x = |x_1 - x_2|$.

In order to eliminate the constants C_i , eq. (1), and the power law behaviour from the three-point functions, we directly normalized our estimates of the three-point functions by the corresponding ones of two-point functions. For the direction $r = f$ we get

$$f_{\sigma\sigma\epsilon} \simeq 2^{-\Delta_\epsilon/2} \frac{\langle s_{x_1} s_{x_2} s_{x_3}^2 \rangle - \langle s_{x_1} s_{x_2} \rangle \langle s^2 \rangle}{\langle s_{x_1} s_{x_2} \rangle [\langle s_{x_1}^2 s_{x_3}^2 \rangle - \langle s^2 \rangle^2]^{1/2}} \quad (17)$$

and

$$f_{\epsilon\epsilon\epsilon} \simeq \frac{\langle s_{x_1}^2 s_{x_2}^2 s_{x_3}^2 \rangle - [\langle s_{x_1}^2 s_{x_2}^2 \rangle + \langle s_{x_1}^2 s_{x_3}^2 \rangle + \langle s_{x_2}^2 s_{x_3}^2 \rangle] \langle s^2 \rangle + 2 \langle s^2 \rangle^3}{[\langle s_{x_1}^2 s_{x_3}^2 \rangle - \langle s^2 \rangle^2] [\langle s_{x_1}^2 s_{x_2}^2 \rangle - \langle s^2 \rangle^2]^{1/2}}, \quad (18)$$

where we used that $|x_1 - x_3| = |x_1 - x_2|$. For the direction $r = d$ we get

$$f_{\sigma\sigma\epsilon} \simeq 3^{-\Delta_\epsilon/2} \frac{\langle s_{x_1} s_{x_2} s_{x_3}^2 \rangle - \langle s_{x_1} s_{x_2} \rangle \langle s^2 \rangle}{\langle s_{x_1} s_{x_2} \rangle [\langle s_{x_2}^2 s_{x_3}^2 \rangle - \langle s^2 \rangle^2]^{1/2}} \quad (19)$$

and

$$f_{\epsilon\epsilon\epsilon} \simeq \frac{\langle s_{x_1}^2 s_{x_2}^2 s_{x_3}^2 \rangle - [\langle s_{x_1}^2 s_{x_2}^2 \rangle + \langle s_{x_1}^2 s_{x_3}^2 \rangle + \langle s_{x_2}^2 s_{x_3}^2 \rangle] \langle s^2 \rangle + 2 \langle s^2 \rangle^3}{[\langle s_{x_1}^2 s_{x_3}^2 \rangle - \langle s^2 \rangle^2]^{1/2} [\langle s_{x_2}^2 s_{x_3}^2 \rangle - \langle s^2 \rangle^2]^{1/2} [\langle s_{x_1}^2 s_{x_2}^2 \rangle - \langle s^2 \rangle^2]^{1/2}}. \quad (20)$$

IV. FINITE SIZE EFFECTS

Compared with the linear size L of the lattice, the distances that we consider for our two- and three-point functions are small. In that respect they can all be viewed as operators in the even channel such as the energy density. The free energy density on a finite lattice, for a vanishing external field behaves as [10–13]

$$f(\beta, L) = L^{-d} h(L^{1/\nu} t) + f_{ns}(t), \quad (21)$$

where $t = (\beta_c - \beta)/\beta_c$ is the reduced temperature, h and f_{ns} are analytic functions. Taking the derivative with respect to t we arrive at

$$E(\beta, L) = L^{-d+1/\nu} \tilde{h}(L^{1/\nu} t) + E_{ns}(t), \quad (22)$$

where $\tilde{h} = -h'/\beta_c$. Setting $\beta = \beta_c$ we get

$$E(\beta_c, L) = L^{-d+1/\nu} \tilde{h}(0) + E_{ns}(0), \quad (23)$$

where $d - 1/\nu = d - y_t = \Delta_\epsilon$.

Given the huge amount of data, we abstain from sophisticated fitting with Ansätze motivated by eq. (23). Instead we consider pairs of linear lattice sizes $L_1 = L$, $L_2 = 2L$ and compute

$$G_{ex}(2L) := G(2L) + \frac{G(2L) - G(L)}{2^{\Delta_\epsilon} - 1}, \quad (24)$$

where G is the quantity under consideration.

V. VARIANCE REDUCTION

Here we discuss the construction of variance reduced estimators of N -point functions along the lines of refs. [19, 20] in a general setting. Let us consider the N -point function

$$\langle \mathcal{O}_1(x_1)\mathcal{O}_2(x_2)\dots\mathcal{O}_N(x_N) \rangle = \frac{\int D[\phi] \exp(-H[\phi]) \mathcal{O}_1(x_1)\mathcal{O}_2(x_2)\dots\mathcal{O}_N(x_N)}{\int D[\phi] \exp(-H[\phi])}, \quad (25)$$

where $[\phi]$ denotes the collection of all fields. In the case of the Blume-Capel model that we simulate here, it is actually the collection of the spins s_x and the integral becomes the sum over all configurations. Let us consider subsets $x_i \in \mathcal{B}_i \subset \Lambda$ of sites for each i , where Λ is the set of all sites of the lattice. Typically one takes $x_k \in \mathcal{B}_i$ if $\|x_k - x_i\| \leq l_{max}$ for some norm $\|\cdot\|$. The crucial requirement is that for any pair $i \neq j$, no pair of sites $x_k \in \mathcal{B}_i$ and $x_l \in \mathcal{B}_j$ exists such that x_k and x_l are nearest neighbours. In Fig. 1 we sketch an implementation for a square lattice and three points. For simplicity, in the sketch as well as in our simulations, we use the Chebyshev distance. Let us denote the collection of fields living on \mathcal{B}_i by $[\phi]_i$ and the collection of fields that are not associated with any of the blocks by $[\phi]_R$. The reduced Hamiltonian can be written as sum, where one summand depends only on the fields on the remainder and the others on the fields on the remainder and on one of the blocks:

$$H[\phi] = h_R([\phi]_R) + \sum_i h_i([\phi]_i, [\phi]_R). \quad (26)$$

This decomposition allows us to rewrite the expectation value in the following way:

$$\begin{aligned} & \langle \mathcal{O}_1(x_1)\mathcal{O}_2(x_2)\dots\mathcal{O}_N(x_N) \rangle \\ &= \frac{\int D[\phi]_R \exp[-h_R([\phi]_R)] \int (\prod_i D[\phi]_i) (\prod_i \exp[-h_i([\phi]_i, [\phi]_R)]) (\prod_i \mathcal{O}_i(x_i))}{\int D[\phi]_R \exp[-h_R([\phi]_R)] \int (\prod_i D[\phi]_i) (\prod_i \exp[-h_i([\phi]_i, [\phi]_R)])} \\ &= \frac{\int D[\phi]_R \exp[-h_R([\phi]_R)] \prod_i (\int D[\phi]_i \exp[-h_i([\phi]_i, [\phi]_R)] \mathcal{O}_i(x_i))}{\int D[\phi]_R \exp[-h_R([\phi]_R)] \prod_i (\int D[\phi]_i \exp[-h_i([\phi]_i, [\phi]_R)])} \\ &= \frac{\int D[\phi]_R \exp[-h_R([\phi]_R)] (\prod_i z_i([\phi]_R)) (\prod_i \langle \mathcal{O}_i(x_i) \rangle_i([\phi]_R))}{\int D[\phi]_R \exp[-h_R([\phi]_R)] \prod_i z_i([\phi]_R)}, \end{aligned} \quad (27)$$

where we define

$$z_i([\phi]_R) = \int D[\phi]_i \exp[-h_i([\phi]_i, [\phi]_R)] \quad (28)$$

and

$$\langle \mathcal{O}_i(x_i) \rangle_i([\phi]_R) = \frac{\int D[\phi]_i \exp[-h_i([\phi]_i, [\phi]_R)] \mathcal{O}_i(x_i)}{z_i([\phi]_R)}. \quad (29)$$

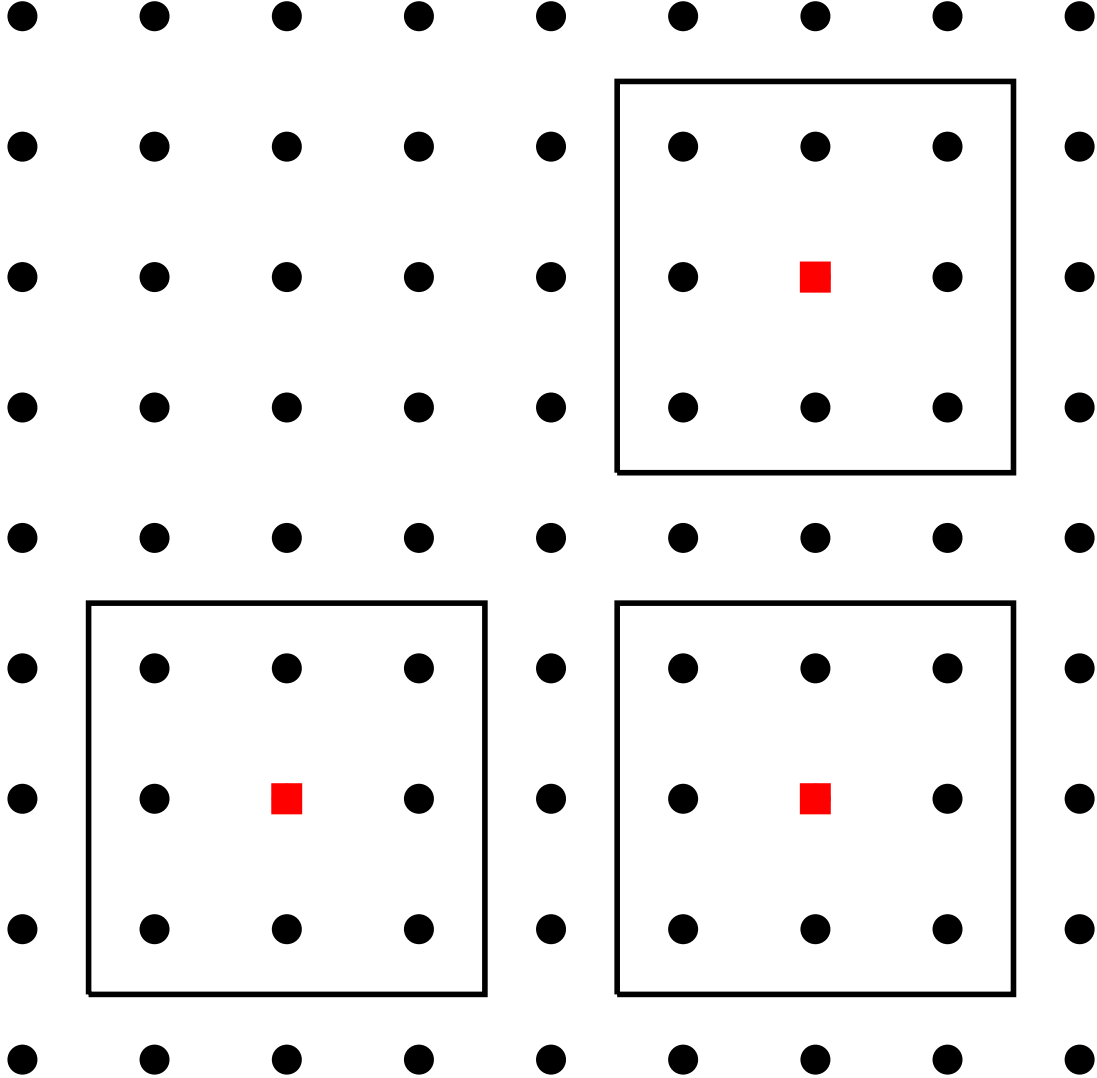


FIG. 1. Two-dimensional sketch of the decomposition of the lattice into blocks and the remained. The three points x_1 , x_2 , and x_3 are represented by red squares. The blocks around these three points are bordered by solid black lines. Lattice sites different from x_1 , x_2 , or x_3 are given by solid black circles.

Note that the variance of $\prod_i \langle \mathcal{O}_i(x_i) \rangle_i$ is smaller than that of $\prod_i \mathcal{O}_i(x_i)$, since degrees of freedom have been integrated out. In our case we can perform an exact summation over all configurations if \mathcal{B}_i is small. In particular if \mathcal{B}_i contains only the site x_i we can easily perform the summation over the three possible values of s_i .

However it is also advantageous to perform the integration over the variables on the blocks \mathcal{B}_i approximately by using a Monte Carlo simulation. Let us denote the simulations

restricted to field variables on the blocks \mathcal{B}_i by baby simulations. These baby simulations are started after the whole system is equilibrated. After the baby simulations are finished, updates on the whole system are performed. Then again baby simulations are started. This process is iterated. During the baby simulations, we perform n_B measurements of $\mathcal{O}_i(x_i)$ for all i . Let us define

$$\overline{\mathcal{O}_i(x_i)_\gamma} = \frac{1}{n_B} \sum_{\alpha=1}^{n_B} \mathcal{O}_{i,\gamma,\alpha}(x_i) \quad , \quad (30)$$

where α labels the measurements that are performed for a given configuration on the remainder. The configurations on the remainder are labelled by γ . We generate n_R configurations on the remainder after equilibration. An estimate of the N -point function is obtained by

$$\overline{\overline{\mathcal{O}_1(x_1)} \overline{\mathcal{O}_2(x_2)} \dots \overline{\mathcal{O}_N(x_N)}} = \frac{1}{n_R} \sum_{\gamma=1}^{n_R} \overline{\mathcal{O}_1(x_1)_\gamma} \overline{\mathcal{O}_2(x_2)_\gamma} \dots \overline{\mathcal{O}_N(x_N)_\gamma} \quad . \quad (31)$$

Let us discuss the variance of $\prod_i \overline{\mathcal{O}_i(x_i)}$. The baby Monte Carlo simulations are independent of each other. Therefore actually n_B^N configurations are generated for the N -point function. Hence, at least for small n_b , we expect that the variance of $\prod_i \overline{\mathcal{O}_i(x_i)}$ behaves as n_B^{-N} . As n_B further increases the variance of $\prod_i \langle \mathcal{O}_i(x_i) \rangle_i$ is approached. Hence the maximal efficiency is reached at some finite n_B that in general has to be determined numerically.

VI. THE ALGORITHM AND OUR IMPLEMENTATION

As in our previous studies of the Blume-Capel model, for example [24], we simulated the model by using a hybrid of the local heat bath algorithm, the local Todo-Suwa algorithm [25, 26], and the single cluster algorithm [27]. The Todo-Suwa algorithm is a local algorithm that does not fulfil detailed balance but only balance. Since ergodicity can not be proved for the Todo-Suwa algorithm, additional local heat bath updates are needed to ensure ergodicity for the update scheme as a whole. The advantage of the Todo-Suwa algorithm is that it reduces autocorrelation times compared with the heat bath algorithm.

A. Implementation

We used the SIMD-oriented Fast Mersenne Twister algorithm [28] as random number generator. Our code is a straight forward implementation of the algorithms in standard

C. We abstained from a parallelization of the algorithms, since in the case of the single cluster update, a good scaling of the performance with the number of processes is hard to achieve, see for example ref. [29]. We stored the value of the spins as character variable. For simplicity we abstain from using a more compact storage scheme, using for example two bits for a spin only. With this setup, on the hardware that is available to us, $L = 1600$ is about the largest linear lattice size that can be simulated efficiently. In order to extrapolate in L and also monitor the dependence of our results on the lattice size we performed simulations for the linear lattice sizes $L = 400, 600, 800, 1200,$ and 1600 .

A cycle of the update consists of one heat bath sweep followed by n_{cl} single cluster updates. Then follow n_{ts} sweeps using the Todo-Suwa algorithm. For each of these sweeps n_{cl} single cluster updates are performed. Mostly n_{cl} is chosen such that, very roughly, n_{cl} times the average cluster size equals the number of sites L^3 . For the range of lattice sizes studied here $n_{cl} = L$ is a reasonable choice.

Let us summarize an update cycle with the following pseudo-C code:

```

heat bath sweep
for(icl=0;icl<ncl;icl++)  single cluster update
for(its=0;its<nts;its++)
{
  Todo-Suwa sweep
  for(icl=0;icl<ncl;icl++)  single cluster update
}
baby simulations for all blocks
measure N-point functions

```

We parallelized trivially by performing several independent runs. The equilibration takes a significant amount of CPU-time for the larger lattices. Therefore, in the case of the linear lattice sizes $L = 800, 1200,$ and 1600 , we first equilibrated a single Markov chain. We started from a disordered configuration. Since in the initial phase of the simulation clusters are small, we adapted the number of cluster updates for the first few update cycles, such that the aggregate cluster size per local update sweep is equal to the lattice volume or larger. After this initial phase, we continued with a fixed number of single cluster updates per local update sweep as discussed above. We performed 1000 complete update cycles to

equilibrate the system. These update cycles are characterized by $n_{ts} = 3$. Here we only measured a few quantities like the energy density and the magnetisation to monitor the equilibration. We stored the final configuration to disc. Then we started several runs using this configuration as initial one and different seeds for the random number generator. In these runs we used $n_{ts} = 9$. Since the baby simulations discussed below take a considerable amount of CPU-time, we intend to essentially eliminate the correlation between subsequent measurements by using such a large number for n_{ts} . In the case of $L = 800, 1200$, and 1600 , starting from the configuration written to disc, we performed four update cycles to achieve a sufficient decorrelation between the branches of our simulation before measuring the N -point functions.

B. The baby Monte Carlos and the measurements

In our simulations we did not attempt to adjust the size of the blocks to the distances between the points in the N -point functions. Instead we determined the N -point functions for a certain range of distances for a given decomposition into blocks.

In order to save CPU-time, we determined $\overline{s_x}$ and $\overline{s_x^2}$ for a subset of the lattice sites only. This subset is characterized by $x^{(i)} = 0, n_s, 2n_s, \dots, L - n_s$. In our study we performed simulations for the strides $n_s = 2$ and 4 . We used blocks around these sites that are defined by $y \in \mathcal{B}_i$ if $|y^{(k)} - x_i^{(k)}| < n_s$ for $k = 0, 1$ and 2 . This means that the linear size of these blocks is $l_b = 3$ and 7 for $n_s = 2$ and 4 , respectively. Before starting the baby simulations we copied the spins of the block and its outer boundary to an auxiliary array. Since for our choice nearest neighbour blocks overlap, we can not write all the final configurations of the baby simulations back to the main Markov chain. Only a subset with the larger stride $2n_s$ could be used to this end. However, for simplicity we refrain to do so. At the end of the baby simulations we only stored the results $\overline{s_x}$ and $\overline{s_x^2}$ to compute the estimates of the N -point functions. We computed the two- and three-point functions for the distances $j = 2n_s, 3n_s, \dots, 9n_s$. Note that for $j = n_s$ the blocks overlap, and no valid result is obtained.

In the case of $n_s = 2$, we performed n_b sweeps over the block using the Todo-Suwa algorithm. Note that in the case of the baby simulations ergodicity is not needed. In preliminary simulations we varied n_b . It turns out that the performance maximum is not very sharp and depends on the type of the N -point function and on the distance j . Based

on these experiments, we decided to use $n_b = 10$ in our production runs.

We performed a measurement for the starting configuration and after each Todo-Suwa sweep. We reduced the variance by performing the sum over s_x for fixed neighbours exactly:

$$\tilde{s}_x = \frac{\sum_{s_x} \exp(\beta s_x S_x - D s_x^2) s_x}{\sum_{s_x} \exp(\beta s_x S_x - D s_x^2)} \quad (32)$$

and

$$\tilde{s}_x^2 = \frac{\sum_{s_x} \exp(\beta s_x S_x - D s_x^2) s_x^2}{\sum_{s_x} \exp(\beta s_x S_x - D s_x^2)}, \quad (33)$$

where

$$S_x = \sum_{y.nn.x} s_y, \quad (34)$$

where $y.nn.x$ means that y is a nearest neighbour of x .

In the case of $n_s = 4$ we used two different updating schemes. Since the measurement is performed at the central site only, it might be useful to update the spins at central sites more often than those at the boundary. To this end, we performed one sweep using the Todo-Suwa algorithm over the full 7^3 block, then follows a sweep over the central 5^3 and finally a sweep over the central 3^3 block. This sequence is repeated n_b times. A measurement using eq. (32,33) is performed for the initial configuration and after each (partial) sweep. This means that $3n_b + 1$ measurements are performed for each baby simulation. After a few preliminary simulations we decided to take $n_b = 30$. We used this scheme for our simulations of lattices of the linear sizes $L = 400$ and 800 .

For $L = 600, 1200,$ and 1600 we performed cluster updates in addition to the sweeps with the Todo-Suwa update. The cluster construction is started from the fixed boundary of the block using the standard delete probability $p_d = \min[1, \exp(-2\beta s_x s_y)]$, where x and y are nearest neighbours. All spins that are not frozen to the boundary are flipped. Here we used $n_b = 20$. It turned out that the cluster update gives little advantage. However it is likely that going to larger n_s this will change. We made no attempt to construct cluster improved estimators of s_x and s_x^2 .

We performed simulations of the Ising model for $L = 400$ and 800 and $n_s = 2$. In the baby Monte Carlos, we replaced the Todo-Suwa update by the Metropolis one. In the main Markov chain, we replaced the Todo-Suwa sweeps by heat bath sweeps. Note that in the case of the Ising model, the single cluster algorithm is ergodic and it is not necessary to add heat bath sweeps.

TABLE I. *Statistics of our simulations of the Blume-Capel model at $D = 0.655$ and $\beta = 0.387721735$. For a discussion see the text.*

L	$n_s = 2$	$n_s = 4$
400	239510	74270
600	93150	17810
800	39920	15670
1200	10300	1800
1600	4190	1630

C. Statistics of our simulations

For a given set of parameters n_s and L , we performed 8 up to 20 independent runs. Each running for a month on a single core of the CPU. In table I we summarize the total number of update and measurement cycles performed for each stride n_s and linear lattice size L . We performed preliminary simulations without using the variance reduction method. We abstain from discussing these simulations in detail.

In total our study took about 10 years on a single core of a recent CPU.

VII. NUMERICAL RESULTS

Throughout we used the Jackknife method to compute statistical errors.

A. The two-point functions

First we extracted the dimension of the operators from the two-point functions $g(x)$. To this end, we define an effective exponent by

$$\Delta_{eff}(x, \Delta x) = -\frac{1}{2} \frac{\ln(g(x + \Delta x)/g(x))}{\ln((x + \Delta x)/x)} \quad , \quad (35)$$

where $\Delta x = n_s$, $\Delta x = \sqrt{2}n_s$, and $\Delta x = \sqrt{3}n_s$ for $r = a, f$ and d , respectively. Let us first discuss our results obtained for $g_{r,\sigma\sigma}$. In Fig. 2 we plot results obtained for displacements along the axis and the stride $n_s = 2$. We give results for all linear lattice sizes that we

have simulated. Up to our largest linear lattice size $L = 1600$ we see a dependence on the lattice size. In addition we give extrapolated results using the pairs of lattice sizes (400, 800), (600, 1200), and (800, 1600). The extrapolated results are essentially consistent among each other, confirming the validity of the extrapolation. It seems plausible that the extrapolated result approaches the bootstrap value as x increases.

In Fig. 3 we give results for the extrapolation of the pair $(L, 2L) = (800, 1600)$ for all three directions that we have studied. The small x deviations are the largest for $r = a$. For $r = f$ and d they have the opposite sign as for $r = a$. The amplitude of corrections is the smallest for $r = f$. Since the corrections depend strongly on r , it is likely that they are dominantly caused by the breaking of the rotational symmetry and fall off like $x^{-\omega_{NR}}$.

Here we make no effort to extract an optimal estimate for Δ_σ from our data. Just looking at the figure, one might take the result for direction f at distance $x = 10\sqrt{2}$ as final estimate: $\Delta_\sigma = 0.5177(3)$. Using $\eta = 0.03627(10)$ [6], we get $\Delta_\sigma = (1 + \eta)/2 = 0.51814(5)$, which is consistent, but clearly more accurate. In the following analysis we shall use the bootstrap value $\Delta_\sigma = 0.5181489(10)$, which outpaces the Monte Carlo results by far.

Let us look in more detail at the corrections at small distances. Since we study an improved model, we expect that the numerically dominant corrections are due to the breaking of the Galilean invariance by the lattice. In Fig. 4 we plot our extrapolated results for $g_{\sigma\sigma}x^{2\Delta_\sigma}$ with $\Delta_\sigma = 0.5181489$ for the three directions studied. We have fitted these data with

$$x^{2\Delta_\sigma}g_{r,\sigma\sigma}(x) = c + a_r x^{-\omega_{NR}} \quad (36)$$

with $\omega_{NR} = 2.022665$. For simplicity, we performed a naive fit of the data, not taking into account the statistical correlation of the data for different distances and directions. We fitted jointly the data for the three different directions, requiring that the constant c is the same for all three directions. The result is represented by the solid lines in Fig. 4. Given the shortcomings of the fit we do not give final results for the constants c and a_r . Our aim is to demonstrate that the Ansatz (36) indeed describes the data well as can be seen in the plot.

Next we analysed the $\epsilon\epsilon$ function. The findings are analogous to those of the $\sigma\sigma$ function. Therefore we refrain from a detailed discussion. A main difference is that the relative statistical error increases faster as for the $\sigma\sigma$ function. In Fig. 5 we have plotted the

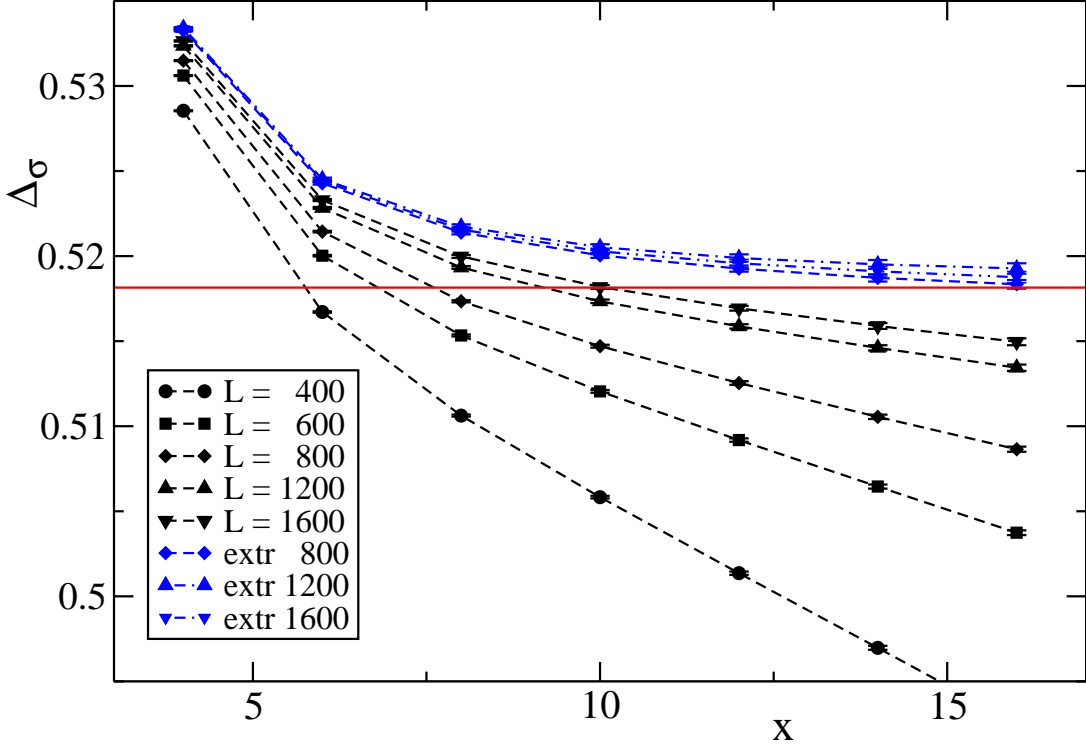


FIG. 2. We plot the effective dimension $\Delta_{\sigma,eff}(x, s)$ of the field as defined by eq. (35) for various linear lattice sizes L and extrapolated estimates. The displacement between the points is in direction $r = a$. The dashed lines should only guide the eye. We give only results obtained from our simulations with stride $n_s = 2$ to keep the figure readable. The horizontal solid line gives $\Delta_\sigma = 0.5181489$ obtained by the bootstrap method.

analogue of Fig. 4.

B. The three-point functions

Let us first check that the extrapolation in the lattice size works. To this end we plot in Fig. 6 our estimates of $f_{\sigma\sigma\epsilon}$ for $r = f$, eq. (17), as a function of the distance x for different linear lattice sizes L . In addition we give the results obtained from the extrapolation (24). Note that we applied eq. (24) to our estimates of $f_{\sigma\sigma\epsilon}$ obtained for given L . For the results obtained for a given lattice size, we see a clear dependence on the lattice size. In contrast, the extrapolated results are consistent among each other.

In Fig. 7 we plot our results for $f_{\sigma\sigma\epsilon}$ obtained from the extrapolation using the lattice sizes

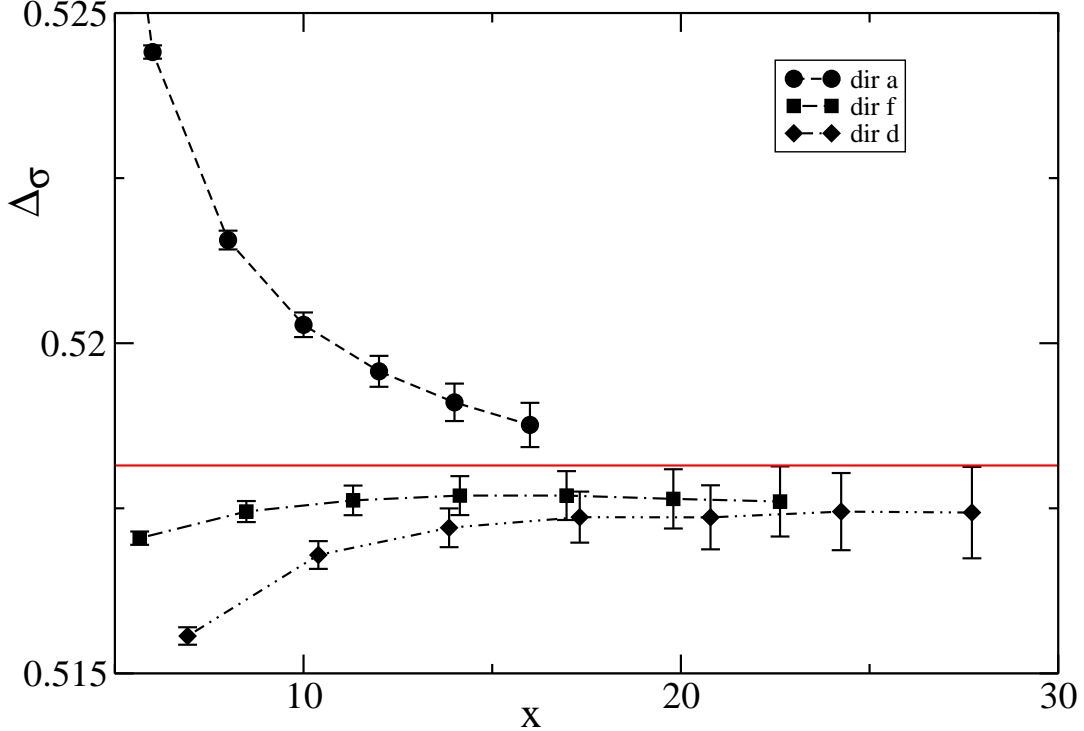


FIG. 3. We plot the effective dimension $\Delta_{\sigma,eff}(x, s)$ of the field as defined by eq. (35) for the extrapolation obtained for $L = 800$ and 1600 . All results are obtained for the stride $n_s = 2$. We give results for all three directions of the displacement that we have studied. The dashed lines should only guide the eye. The horizontal solid line gives $\Delta_{\sigma} = 0.5181489$ obtained by the bootstrap method.

$(L, 2L) = (800, 1600)$. We give results for both geometries that we have implemented. Here we use both the simulations with stride $n_s = 2$ and $n_s = 4$. For distances, where data from both strides are available, we give the weighted average. Throughout, the estimates from $n_s = 2$ are more accurate than those obtained from $n_s = 4$. For example for $r = f$ we get for the distance $j = 16$ the estimates $1.05322(59)$ and $1.05242(88)$ from the simulations with stride $n_s = 2$ and $n_s = 4$, respectively. Also here we see corrections at short distances. We fitted with the Ansatz (36). For simplicity we did not take into account the cross correlations for different distances. We performed independent fits for both directions. Good fits are obtained starting from $j_{min} = 6$, where all $j \geq j_{min}$ are included. For example, for $j_{min} = 8$ we find $c = 1.0513(3)$ and $c = 1.0506(5)$ for $r = f$ and d , respectively. The errors give only an indication, since cross correlations of the data are not taken into account in the fit. In

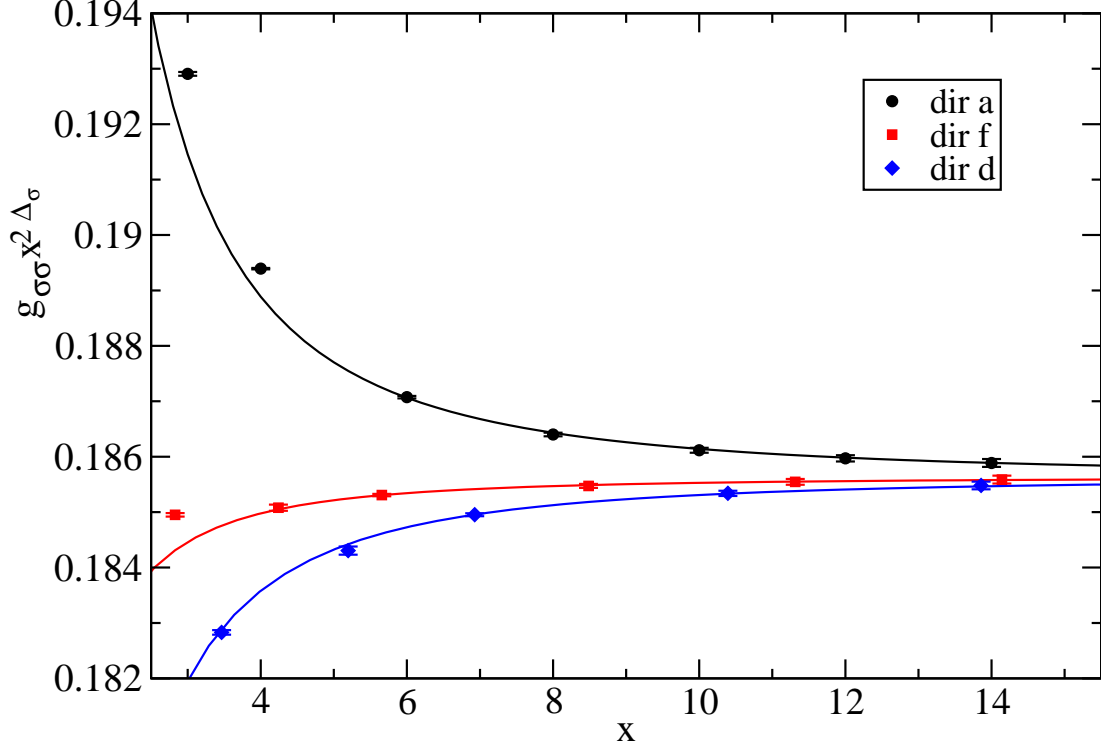


FIG. 4. We plot $g_{\sigma\sigma}x^{2\Delta_\sigma}$ with $\Delta_\sigma = 0.5181489$ for the three directions studied. Most of the data are taken from the simulations with the stride $n_s = 2$. A few data at small distances are taken from our preliminary simulations without variance reduction. The solid lines give the result of the fit with the Ansatz (36).

Fig. 7 results of these fits are given as solid lines.

It is hard to quote a final value that is not biased by the knowledge of the bootstrap result. But it is quite clear that our numerical data are consistent with the bootstrap result. Looking at Fig. 7 we might read off

$$f_{\sigma\sigma\epsilon} = 1.051(1) \quad (37)$$

from the estimate of $f_{\sigma\sigma\epsilon}$ at distances $x \approx 30$, without relying on the fits discussed above.

Next we discuss our results obtained for $f_{\epsilon\epsilon\epsilon}$. Here the statistical error increases faster with the distance than for $f_{\sigma\sigma\epsilon}$. Furthermore we find that our results obtained for the simulations with the stride $n_s = 4$ are more accurate than those with $n_s = 2$. For example for $r = f$ and $j = 16$ we get $f_{\epsilon\epsilon\epsilon} = 1.53089(85)$ and $1.53363(27)$ from our simulations with $n_s = 2$ and $n_s = 4$, respectively. Performing fits with the Ansatz (36) we get for $j_{min} = 8$ the results $c = 1.5312(14)$ and $c = 1.5333(22)$ for $r = f$ and d , respectively.

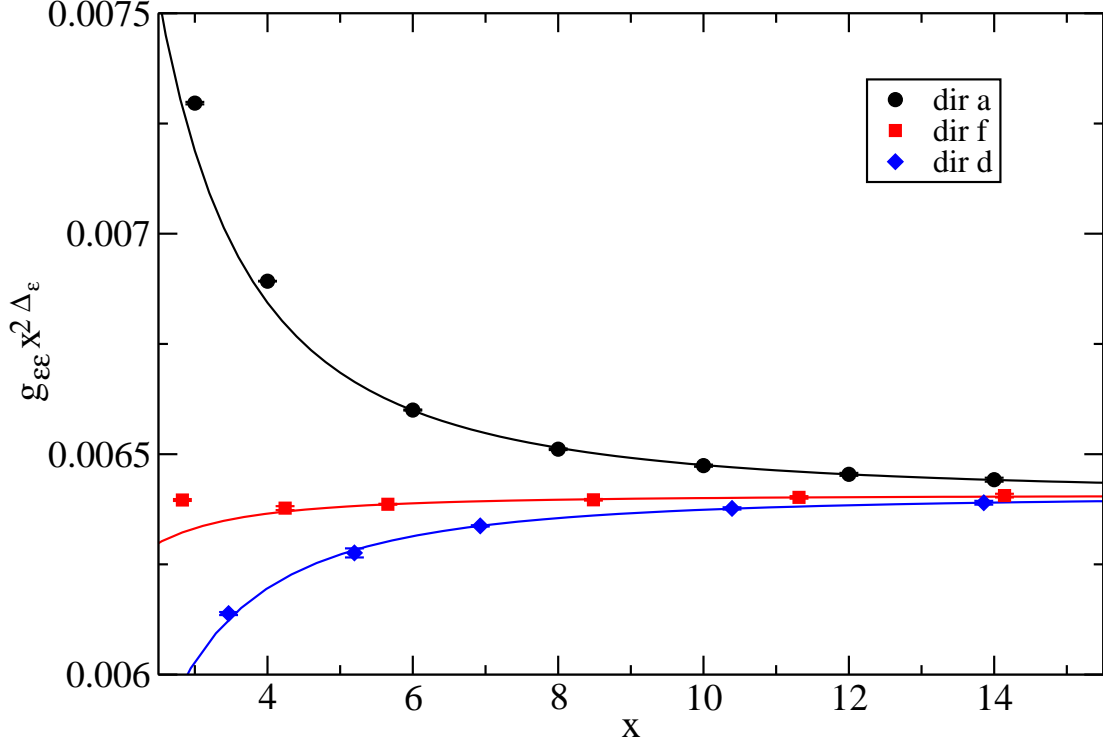


FIG. 5. We plot $g_{\epsilon\epsilon} x^{2\Delta_\epsilon}$ with $\Delta_\epsilon = 1.412625$ for the three directions studied. Analogous to Fig. (4).

In Fig. 7 the results of these fits are given as solid lines. As final result we read off from distances $x \approx 25$

$$f_{\epsilon\epsilon\epsilon} = 1.533(5) \quad (38)$$

not relying on the fits with Ansatz (36).

C. Statistical errors

We find that the relative statistical error of the two-point and three-point functions increases following a power law. The exponent is the same for $n_s = 2$ and $n_s = 4$ and for the simulations without variance reduction. The smallest exponent ≈ 1.36 is found for the $\sigma\sigma$ function and the largest ≈ 4 for the estimate of $f_{\epsilon\epsilon\epsilon}$. This corresponds to the fact that we see the largest gain by using the variance reduction method in the case of $f_{\epsilon\epsilon\epsilon}$.

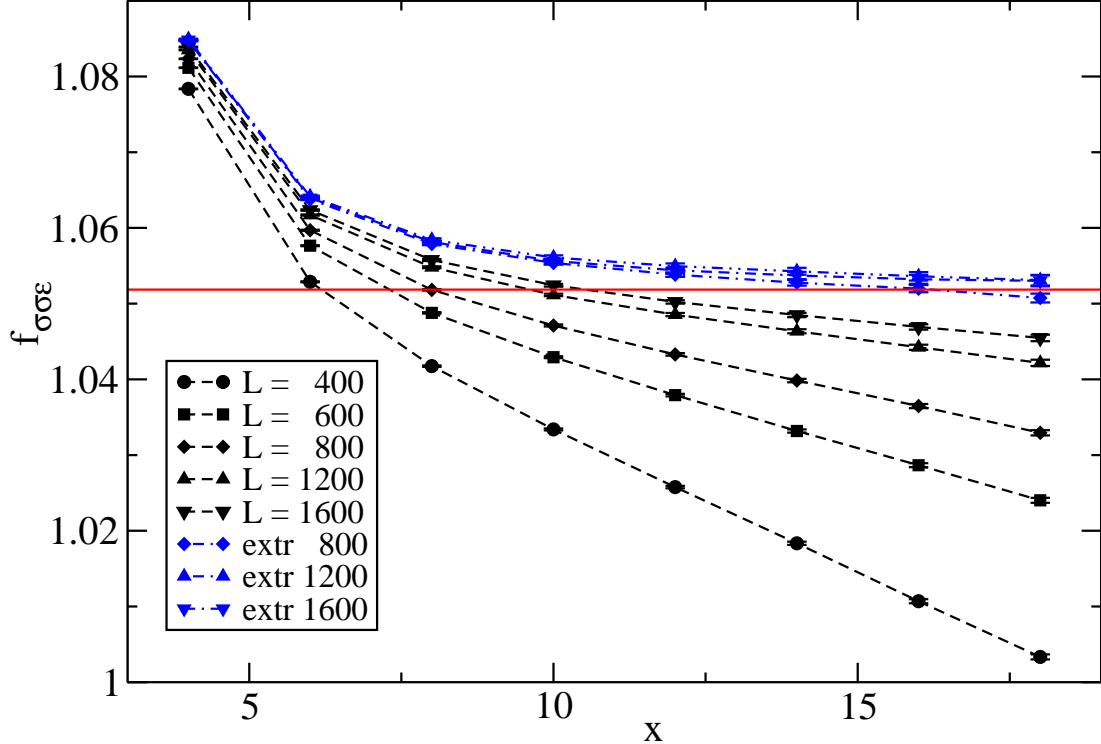


FIG. 6. We plot our estimates of $f_{\sigma\sigma\epsilon}$ for the direction $r = f$. We give results obtained for the linear lattice sizes $L = 400, 600, 800, 1200,$ and 1600 and the extrapolations for the pairs $(L, 2L) = (400, 800), (600, 1200),$ and $(800, 1600)$. All data shown are based on our simulations with $n_s = 2$. The straight line gives the bootstrap result.

D. Sensitivity on the value taken as estimate of β_c

We performed simulations for $L = 800$ with stride $n_s = 2$ at $\beta = 0.38772$ and 0.38772347 in order to estimate the dependence of the N -point functions on β . For $f_{\sigma\sigma\epsilon}$ and $f_{\epsilon\epsilon\epsilon}$, we find that the slope increases with increasing distance. In the case of $f_{\sigma\sigma\epsilon}$ we find an exponent ≈ 1.25 , while for $f_{\epsilon\epsilon\epsilon}$ we get an exponent ≈ 1.38 . From the data it is not completely clear, whether the exponents are different. We estimate that the uncertainty of the estimate $\beta_c = 0.387721735(25)$ used here results in an uncertainty in the fourth digit of $f_{\sigma\sigma\epsilon}$ and $f_{\epsilon\epsilon\epsilon}$ which is negligible compared with the errors quoted above.

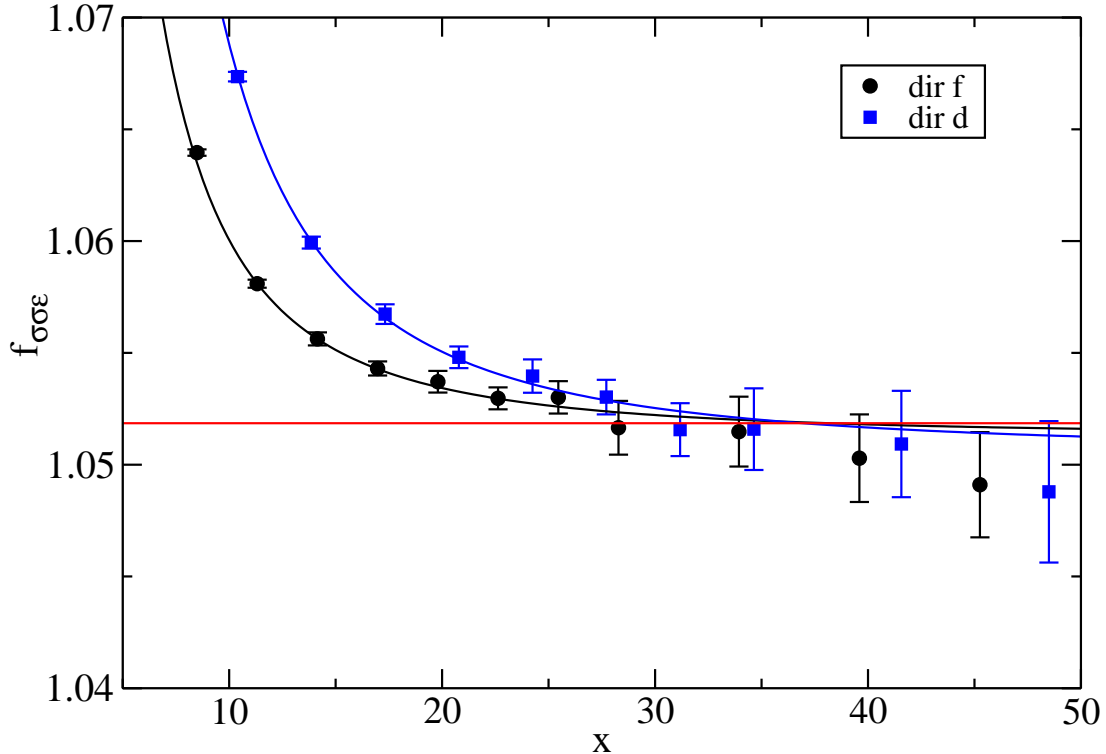


FIG. 7. We plot our estimates of $f_{\sigma\sigma\epsilon}$ as a function of the distance x . These estimates are obtained by the extrapolation of the pair of lattice sizes $(L, 2L) = (800, 1600)$. The solid lines represent the results of fits with the Ansatz (36).

E. Sensitivity on leading corrections

Since we do not know the value of D^* exactly, our results might be affected by residual leading corrections to scaling. In ref. [6] we have demonstrated that the amplitude of leading corrections to scaling should be at least reduced by a factor of 30 in the Blume-Capel model at $D = 0.655$ compared with the Ising model. Therefore we performed simulations of the Ising model at β_c , the pair of lattice sizes $L = 400$ and $L = 800$ and the stride $n_s = 2$. A bit to our surprise, it is hard to see a difference between the results obtained from the Ising model and the improved Blume-Capel model. We conclude that the effects of leading corrections to scaling can be ignored at the level of our accuracy of our final results for $f_{\sigma\sigma\epsilon}$ and $f_{\epsilon\epsilon\epsilon}$.

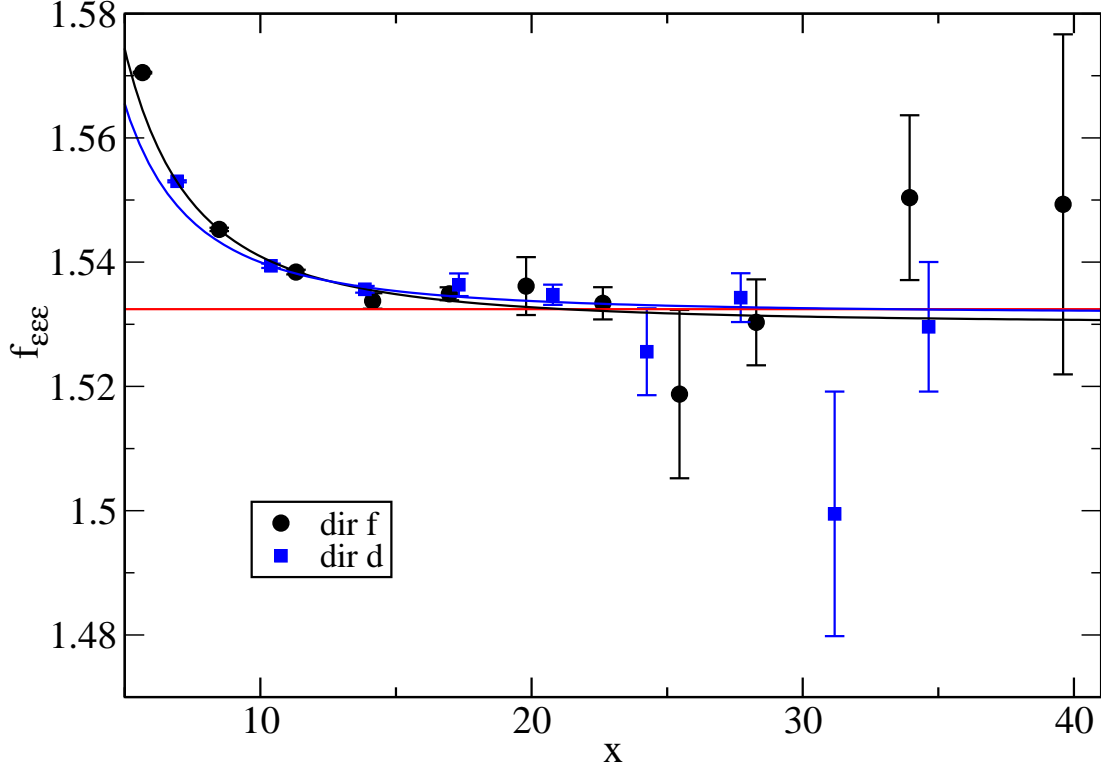


FIG. 8. We plot our estimates of $f_{\epsilon\epsilon\epsilon}$ as a function of the distance x . The solid lines give the results of fits with the Ansatz (36).

VIII. SUMMARY AND CONCLUSIONS

We computed the operator product expansion coefficients $f_{\sigma\sigma\epsilon}$ and $f_{\epsilon\epsilon\epsilon}$ by using Monte Carlo simulations of the improved Blume-Capel model at the critical point. We simulated lattices with periodic boundary conditions up to a linear size $L = 1600$. We extrapolated our results assuming that finite size corrections vanish $\propto L^{-\Delta_\epsilon}$, where L is the linear size of the lattice. An important ingredient of our study is the variance reduced estimator based on [19, 20]. In particular $f_{\epsilon\epsilon\epsilon}$ could be determined accurately due to the variance reduction. The error of our results is smaller than that of previous estimates obtained by Monte Carlo simulations of the three-dimensional Ising model.

Our results are fully consistent with the predictions obtained by the conformal bootstrap method. These results are however by far more accurate than ours. Our study still can be understood as preliminary. Easily more CPU time could be used and the parameters of the algorithm could be better tuned. However one would hardly reach the accuracy

obtained by using the conformal bootstrap method. The fact that our results agree with those of the conformal bootstrap method confirm the theoretical expectation that the RG fixed point that governs the three-dimensional Ising universality class is indeed invariant under conformal transformations.

The strategy used here seems to be applicable to other universality classes. However in the case of $O(N)$ -symmetric model with $N \geq 2$ more memory per site is needed and therefore the linear lattice sizes that can be reached are smaller. It is unclear, whether these lattice sizes allow for a reliable extrapolation to the infinitely large system.

An interesting idea would be to combine the UV-sampler [17, 18] or some similar method with the variance reduced estimator of N -point functions discussed here.

IX. ACKNOWLEDGEMENT

This work was supported by the DFG under the grant No HA 3150/4-1.

-
- [1] F. Kos, D. Poland, and D. Simmons-Duffin, JHEP **11**, 109 (2014), arXiv:1406.4858 [hep-th].
 - [2] F. Gliozzi and A. Rago, JHEP **10**, 042 (2014), arXiv:1403.6003 [hep-th].
 - [3] F. Kos, D. Poland, D. Simmons-Duffin, and A. Vichi, JHEP **08**, 036 (2016), arXiv:1603.04436 [hep-th].
 - [4] D. Simmons-Duffin, JHEP **03**, 086 (2017), arXiv:1612.08471 [hep-th].
 - [5] D. Simmons-Duffin, in *Proceedings, Theoretical Advanced Study Institute in Elementary Particle Physics: New Frontiers in Fields and Strings (TASI 2015): Boulder, CO, USA, June 1-26, 2015* (2017) pp. 1–74, arXiv:1602.07982 [hep-th].
 - [6] M. Hasenbusch, Phys. Rev. **B82**, 174433 (2010), arXiv:1004.4486 [cond-mat.stat-mech].
 - [7] M. Campostrini, A. Pelissetto, P. Rossi, and E. Vicari, Phys. Rev. **E65**, 066127 (2002), arXiv:cond-mat/0201180 [cond-mat].
 - [8] P. Butera and M. Comi, Phys. Rev. **B72**, 014442 (2005), arXiv:hep-lat/0506001 [hep-lat].
 - [9] R. Guida and J. Zinn-Justin, J. Phys. **A31**, 8103 (1998), arXiv:cond-mat/9803240 [cond-mat].
 - [10] K. G. Wilson and J. B. Kogut, Phys. Rept. **12**, 75 (1974).

- [11] M. E. Fisher, *Rev. Mod. Phys.* **46**, 597 (1974), [Erratum: *Rev. Mod. Phys.*47,543(1975)].
- [12] M. E. Fisher, *Conceptual foundations of quantum field theory. Proceedings, Symposium and Workshop, Boston, USA, March 1-3, 1996*, *Rev. Mod. Phys.* **70**, 653 (1998).
- [13] A. Pelissetto and E. Vicari, *Phys. Rept.* **368**, 549 (2002),
arXiv:cond-mat/0012164 [cond-mat].
- [14] A. M. Polyakov, *JETP Lett.* **12**, 381 (1970), [*Pisma Zh. Eksp. Teor. Fiz.*12,538(1970)].
- [15] M. Caselle, G. Costagliola, and N. Magnoli, *Phys. Rev.* **D91**, 061901 (2015),
arXiv:1501.04065 [hep-th].
- [16] G. Costagliola, *Phys. Rev.* **D93**, 066008 (2016), arXiv:1511.02921 [hep-th].
- [17] V. Herdeiro, *Phys. Rev. E* **96**, 033301 (2017), arXiv:1705.11045 [cond-mat.stat-mech].
- [18] V. Herdeiro and B. Doyon, *Phys. Rev.* **E94**, 043322 (2016),
arXiv:1605.05350 [cond-mat.stat-mech].
- [19] G. Parisi, R. Petronzio, and F. Rapuano, *Phys. Lett.* **128B**, 418 (1983).
- [20] M. Lüscher and P. Weisz, *JHEP* **09**, 010 (2001), arXiv:hep-lat/0108014 [hep-lat].
- [21] Y. Deng and H. W. J. Blöte, *Phys. Rev. E* **70**, 046111 (2004).
- [22] M. Hasenbusch, *Int. J. Mod. Phys. C* **12**, 911 (2001).
- [23] M. Hasenbusch, *Phys. Rev. B* **85**, 174421 (2012), arXiv:1202.6206 [cond-mat.stat-mech].
- [24] M. Hasenbusch, *Phys. Rev. E* **93**, 032140 (2016), arXiv:1512.02491 [cond-mat.stat-mech].
- [25] S. Todo and H. Suwa, *J. Phys.: Conf. Ser.* **473**, 012013 (2013),
arXiv:1310.6615 [cond-mat.stat-mech].
- [26] F. Gutsch, *Markov-Ketten ohne detailliertes Gleichgewicht*, Bachelor thesis, Humboldt-Universität zu Berlin (2014).
- [27] U. Wolff, *Phys. Rev. Lett.* **62**, 361 (1989).
- [28] M. Saito and M. Matsumoto, “SIMD-oriented Fast Mersenne Twister: a 128-bit Pseudorandom Number Generator”, in *Monte Carlo and Quasi-Monte Carlo Methods 2006*, edited by A. Keller, S. Heinrich, H. Niederreiter, (Springer, 2008); M. Saito, Masters thesis, Math. Dept., Graduate School of science, Hiroshima University, 2007. The source code of the program is provided at “<http://www.math.sci.hiroshima-u.ac.jp/~m-mat/MT/SFMT/index.html>”
- [29] J. Kaupužs, J. Rimšāns, and R. V. N. Melnik, *Phys. Rev. E* **81**, 026701 (2010).